Analysis of Active Reflection Coefficient and Radiated Fields on a Co-Located MIMO Radar System in Transmit Mode

Nivia Colon-Diaz* **and Dan Janning**

Abstract—A study of the impact of coupling effects in a co-located multiple input multiple output (MIMO) radar system is presented. Predicted and measured results corroborate that the active reflection coefficient (ARC) and beampatterns are impacted by the excitation of each sub-array, the geometric configuration, and their polarization. A uniform linear array (ULA) and a uniform planar array (UPA) layouts are considered. The excitations used in the study are linear frequency modulation (LFM) and Doppler division multiple access (DDMA). A thorough analysis is presented to understand the effects these parameters have on the ARC and on the beampatterns of the radar system.

1. INTRODUCTION

The current trend is to develop multiple-input multiple-output (MIMO) radar systems capable of performing simultaneous radar and communication functions. The reason for doing so is apparent; one realizes significant gains in both the footprint of the device as well as functionality. In fact, the advances of MIMO radar systems are motivated by the development of unmanned, attritable, low cost vehicles, which have limitations in cost, size, weight and power (C-SWaP). These low-cost agile vehicles require sensors capable of performing multiple functionalities (i.e., communications, ground moving target identification (GMTI), synthetic aperture radar (SAR), etc.). Combining several sensors into one multifunctional sensor capable of performing simultaneous functionalities has been proven effective to relax C-SWaP constraints [1]. But practical realization of such systems faces a significant bottleneck. The key to effectively embed a multifunctional MIMO sensor on a small, low-cost, attritable vehicle is to understand the coupled power performance of different sub-systems and the impact of this coupling on the function of the module.

Understanding the impact on performance due to the coupled power between functions is imperative for hardware design and function management of such MIMO systems and its waveforms. A co-located MIMO radar system is typically formed by electrically close-networked subarrays performing low power applications such as radar and communications or high power applications such as electronic warfare. In the latter scenario, it stands to reason that there is a potential to damage the radio frequency (RF) system's transmitter due to unexpected coupled power between the networked subarrays [2]. As a result, the analysis and development of methodologies to assess the coupled power impact on co-located MIMO radar performance is of great importance.

However, this problem, while easily stated, is not trivial. To properly capture the impact of coupled power, one needs to include sufficient physical phenomenology for assessing coupling in multi-functional systems and its impact on performance. The characterization of coupled power demands (a) higher fidelity modeling of antenna element type, geometrical configuration, and polarization; (b) measurement of the reverse and forward waves to calculate the active reflection coefficient, the total beam pattern in the far field when the system is executing simultaneous functions; and (c) analysis technique to estimate

* Corresponding author: Nivia Colon-Diaz (nivia.colon_diaz.3@us.af.mil).
The authors are with the Air Force Research Laboratory, USA.

the active voltage standing wave ratio (VSWR) and the performance degradation of the simultaneous functions due to coupled power. As is evident, this holistic understanding of fully coupled MIMO radar systems is challenging. As a result, most of the analysis are piecemeal. Some considered multi-functionally ignoring coupled power, others assessed mutual coupling but for single functionality like angle of arrival. Very few consider multi-functionality and coupled power. To contextualize our research, we provide a brief overview of work that has been done in the past. We note that this review is not intended to be comprehensive.

Pioneers in the field of multi-functionality have enhanced the state-of-the-art by combining simultaneous radar and communication functions utilizing multi-beam radar and communications waveform design [3], incorporating tandem-hopped techniques for embedding communication signals on radar functions [4, 5], and applying waveform optimization techniques to increase joint radar and communications performance [6–9].

Others have demonstrated the feasibility of a joint radar-communications receiver used for communications and synthetic aperture radar functions [10], and the implementation with software defined radios [11], deriving bounds and concepts for multi-functionality [12, 13], introducing metrics [14] and system performance [15, 16] for the spectrum sharing problem analysis between radar and communications [17]. The work of [18–20] provide a comprehensive overview and a starting point to researchers working on these areas.

While the literature referred to thus far dealt with multifunctional systems, there has also been work dedicated to understand mutual coupling on systems performing single functions in passive mode. For instance, the assessment of mutual coupling effects on the performance of adaptive arrays has been done in Refs. [21–23], while that on phased arrays for direction finding can be found in [24–26].

When dealing with single functions in active mode, Pozar [27] used the active reflection coefficient (ARC) as a metric for assessing phased array performance, whereas [28] applied the active input impedance of the elements as a function of scanning angle.

The realization that one needs a more complete full coupled solution, or a solution wherein the operation is correlated to both power and spatial coupling is more recent. Few researchers have addressed the coupling effects for co-located multifunction MIMO radar systems. For instance, Babur et al. [29] stressed the importance of understanding the impact of mutual coupling on MIMO in active mode and its effect with space time codes radiated signals and validated results with using a linear array of patch radiators. Next, Arnold [30] developed a mathematical model that quantifies the effects of mutual coupling from a uniform linear array (ULA) of dipoles on target detection performance of a MIMO radar using orthogonal excitations. Schmid et al. [31] incorporated calibration techniques on MIMO radar systems using frequency modulated continuous wave (FMCW) to compensate for mutual coupling effects on side-lobe levels. The first examination of random coded binary excitations was introduced by Savy and Lesturgie [32] while analyzing their impact on mutual coupling using the concepts from [27] to explore the ARC, active VSWR, and element pattern concepts on a ULA of dipoles only.

Colon-Diaz et al. [33] extended Savy's approach applying computational electromagnetics (CEM) to compute the ARC from any type of antenna element and [34] used dual directional couplers (DDC) to obtain direct measurements of the forward and reverse waves, proportional to the coupled power, on each radiator of a dipole array. The methodology described provides a more direct estimate of the ARC, defined as the ratio of the reflected and incident signals to element n when all the ports are excited. The DDCs were used to collect simultaneous measurements of reverse and forward waves at each channel to estimate the ARC. While Colon-Diaz used DDCs to **simultaneously** measure reverse and forward waves, Zhang et al. [35] developed a methodology more suitable for phased arrays using a directional coupler. The work equally feeds each element the same incident wave through the use of a power division network while collecting the reverse wave of one element at a time. To extend [34] Colon-Diaz et al. in [36] controlled the degradation caused by the coupling effects with a waveform designed to limit the coupling between the elements to a given value.

There have been many advances in this area, but several topics remain to be studied, particularly for multifunction MIMO radar systems. Specifically, one needs to understand performance variations reflected on the expected total transmitted fields and the coupled power in electrically closed networked elements due to (1) the inter-element spacing; (2) geometric configuration; (3) polarization; and (4) the type of simultaneously transmitted waveforms. Addressing these issues is the goal of this paper.

Specifically, the contributions of this paper are as follows. We will: (1) extend the methodology from [33] to predict the total transmitted fields in the far field for arbitrary radiating elements and geometrical configuration; (2) generalize the methodology from [34] to record simultaneous reverse and forward waves of a co-located MIMO radar when simultaneously excited with different waveforms; (3) assess the performance impact of the total radiated fields for different cases; (i) with arbitrary waveforms (linear frequency modulated (LFM) and Doppler division multiple access (DDMA)); (ii) for linear and planar array of patch antennas; and (iii) for horizontal and vertical polarizations; (4) assess the performance impact of the ARC for LFM case, and (5) upgrade the Air Force Research Laboratory (AFRL) co-located MIMO radar testbed, to obtain real data of the total radiated fields and ARC and the validation of the analytical methodology for the cases described above.

The remaining of this paper is organized as follows: Section 2 provides a description of the Baseband-digital at Every Element MIMO Experimental Radar (BEEMER) system, an AFRL MIMO radar testbed [37] used to record measurements and the experiment configuration. In Section 3, we will expand on the method followed to predict the ARC and beampatterns. Section 4 describes the four different sets of waveforms used for the analysis and Section 5 summarizes and concludes the work.

2. FIRMWARE-TUNED, SOFTWARE DEFINED MIMO RADAR TESTBED AND EXPERIMENT CONFIGURATION

In what follows, we will describe the radar testbed, different experimental configurations, the data measured, and finally, how it is processed. While we provide as much data as possible, we will defer to published data when available. In all experiments discussed in this paper, we use the BEEMER reconfigurable radar testbed as it provides the necessary flexibility to study MIMO radar algorithms and waveforms. In this testbed, there is an analog-to digital converter at every element that supports element-level digitization on receive, for digital beamforming, and element level waveform generation on transmit for MIMO waveforms [37]. In Table 1, we summarize the main parameters of the BEEMER system. Briefly, its capabilities are as follows; (a) it supports antennas operating from 70–6000 MHz; (b) its primary components are the ZC706, a field-programmable gate array (FPGA), and (c) the FMCOMMS5, an 8-channels board. The FPGA pre-processes data from a raw signal data format and that is then transferred to the radar signal processing software to extract the information for the user. The FMCOMMS5 is an RF device supporting up to 40 MHz of instantaneous bandwidth, able to receive and transmit from different antenna elements. The testbed is capable of providing more than 8 channels by synchronizing multiple ZC706's/FMCOMMS5's with a bandwidth of 500 MHz.

Table 1. Summary of BEEMER performance metrics [37].

| Parameter	Units	Minimum	Nominal	Maximum
Sampling rate	Mega Samples per Second (MS/s)	-	40	60
Transmitted signal length	Samples	1	-	4096
Center frequency	MHz	70	-	6000
Transmit power	dBm	-	−8	0

We synchronized three boards (each with one ZC706 and one FMCOMMS5). These boards provide a total of 24 channels; however, we only employed 19 channels. Eighteen of them (6 for transmit and 12 for receive) were connected to six dual directional couplers (DDCs) and one was connected to a far field receive antenna, presented in Fig. 1. The remaining 5 unused BEEMER channels were matched terminated. The DDCs used for this work are Hewlett Packard 777D with 1.9–4 GHz frequency band and −20 dB coupling factor, shown in Fig. 2. In this work, the use of a DDC allowed us to collect measurements of reverse and forward waves at each channel. The calibrated ratio between the reverse and forward waves is proportional to the coupled power on each radiator or antenna element. This methodology was previous work developed in [34].
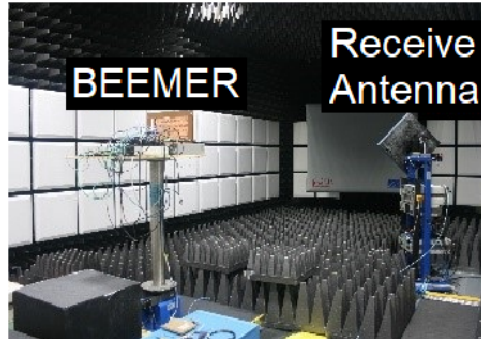
Figure 1. BEEMER system configuration in the anechoic chamber. The back-end of BEEMER, the DDCs, and the UPA are seen on the left while the antenna collecting far-field beampattern data is shown on the right.

Figure 2. Hewlett Packard 777D 1.9–4 GHz with -20 dB coupling factor. '1' represents the input port, '2' represents the forward coupled port, '3' represents the reverse coupled port, and '4' represents the output port. (Figure obtained from www.keysight.com).
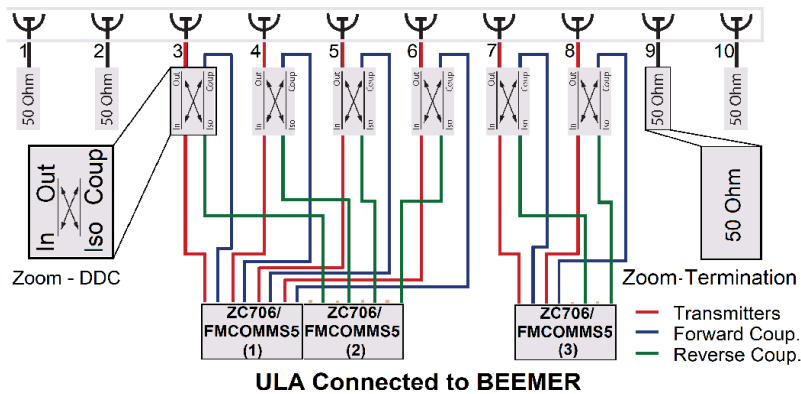

Figure 3. BEEMER system and DDC connections to directly collect ARC measurements. The ZC706 is an FPGA board and each FMCOMMS5 is a 4-channel transceiver.

On a DDC, the majority of the input signal through port '1' will be transmitted out of port '4', with a small sample of the signal captured at port '2'. In a similar manner, a signal coming from port '4' will be transmitted out of port '1' with a small sample collected at port '3'. We use the DDCs connected to BEEMER to simultaneously transmit all arbitrary waveforms, and collect forward and reverse waves. Note, that a reverse wave has a contribution from a self-reflected wave and the coupled waves from networked elements. A more detailed description of the connection between BEEMER and DDCs is as follows. Each of the six BEEMER transmit channels will send an arbitrary waveform through the input port '1' of a DDC to an antenna element via port '4', as depicted by the red lines in Fig. 3. Port '2' of the DDCs were connected to 6 receive BEEMER channels to record a sample of the arbitrary waveforms. This sample is referred to hereafter as the forward waves. They are represented by blue lines in Fig. 3. The other 6 BEEMER receive channels were connected to ports '3' of the DDCs to

record a sample of the reverse waves, seen in green lines in Fig. 3. The collected forward and reverse waves were used to estimate the ARC.

The ARC and total radiated fields are used as a metric for assessing the impact of the antenna geometric configuration and polarization. For this, two sub-array configurations were defined, a ULA of 1×6 radiators, as seen in Fig. 4, and a uniform planar array (UPA) of 2×3 radiators, presented in Fig. 5. The ULA and UPA are selected from an antenna front-end of a 6×10 dual-polarized patch array, with horizontal and vertical polarization, shown in Fig. 4. The unused elements and polarization connections of the 6×10 front-end were matched and terminated. The antenna elements of the ULA or UPA (with either vertical or horizontal polarization) were connected to BEEMER through the output port '4' of the DDCs, as mentioned before.
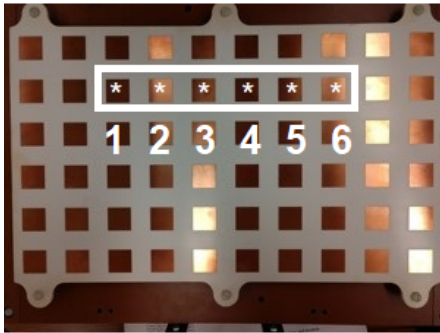
Figure 4. Uniform planar array (UPA) used to collect data (looking from the front of the array). White 'stars' indicate the selected 1×6 sub-array. All other elements were matched terminated.
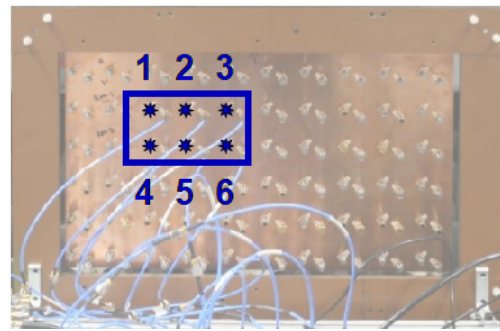
Figure 5. Uniform planar array (UPA) used to collect data (looking from the back of the array). Blue 'stars' indicate the selected 2×3 sub-array. All other elements were matched terminated.

BEEMER recorded far field radiated data for a central frequency of 3.5 GHz, and for different observation angles by moving the transmit antenna front end, placed on top of the positioner at the anechoic chamber (see Fig. 1, in azimuth from $0°$ to $90°$ in steps of $2.5°$ with $0°$ elevation. For a fixed observation angle, arbitrary waveform, geometry configuration, and polarization, BEEMER recorded the excitations, the reverse and forward waves, and the total far field radiated fields.

The data collected is organized in a three dimensional data cube of size $1024 \times 256 \times 19$. The three axes of the data cube are; 1) The samples of a simple pulse or fast time; 2) The repetitions of the pulse or slow time; and 3) The channels. Slow time data was summed (coherently integrated) and pulse compression was applied to the fast time dimension to maximize signal to noise ratio (SNR) in the presence of noise.

As mentioned before, for a fixed geometric configuration, polarization and arbitrary waveform the data recorded from the reverse and forward channels of each antenna element was used to obtain a more direct calculation of the ARC and estimate of the coupled power, and the data collected from the receive antenna was used to form the total radiated fields.

In the next section we will describe the methodology used to predict the ARC applying the measured scattering (S) parameters and the excitations. Measurements of the S-parameters were collected, for both geometric configurations, ULA and UPA, for both horizontal and vertical polarizations following [38]. Additionally, we discuss the approximation utilized for obtaining an estimate of the total far field transmitted fields of an arbitrary MIMO emission.

## 3. ARC AND RADIATED FIELDS OF A CO-LOCATED MIMO RADAR

As described earlier, a MIMO radar system can simultaneously transmit arbitrary waveforms from each digital element or sub-array. It is, therefore, important to understand the impact on performance caused by coupled power between networked elements due to the selected waveforms. MIMO coupled power

effects are assessed through the analysis of the ARC and the total radiated fields. The ARC observed at antenna n is defined as [32]

$$\Gamma_n^a = \frac{b_n}{a_n} = \frac{\sum S_{mn} a_m}{a_n} \qquad (1)$$

where a_m represents the complex amplitude of the forward wave at antenna m; S_{nm} is the S-parameter for a signal incident on port m and measured at port n (when all other ports are matched terminated) [39]; and b_n represents the complex amplitude of the reverse wave at antenna n and has all contributions of the self-reflected wave and coupled waves from all other antennas into antenna n. Thus, Γ_n^a is the ARC observed in antenna n due to the excitations on all other radiators and their coupling with element n [32].

The S-parameters, measured at 3.5 GHz, for the two geometric configurations, ULA and UPA, and for each polarization are shown in the form of heatmaps in Figs. 6–9. The units of the colorbar are dB and they range from -15 dB to -40 dB. Figs. 6–7 show the S-matrix for the ULA with horizontal and vertical polarizations, respectively. Examining Fig. 6 is apparent that the self-coupling values, in orange, are the largest values recorded. And as is apparent that both Figs. 6–7 the coupling reduces as the elements are farther apart, with the lowest value represented in blue. The UPA recorded measurements are shown in Figs. 8–9. For a horizontal polarization, seen in Fig. 8, the largest coupling value is
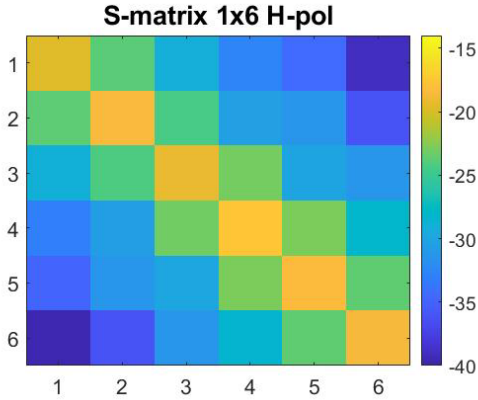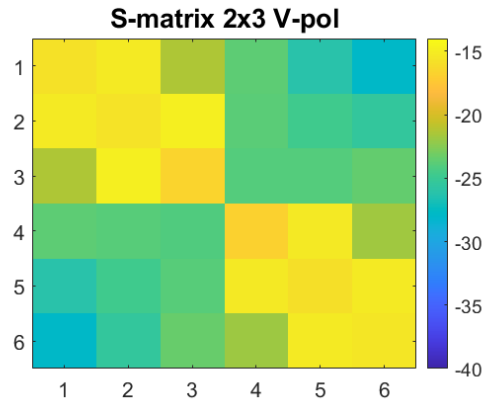

Figure 6. Measured S-matrix for ULA with horizontal polarization. Element numbers displayed in horizontal and vertical axes. Colorbar units in dB.
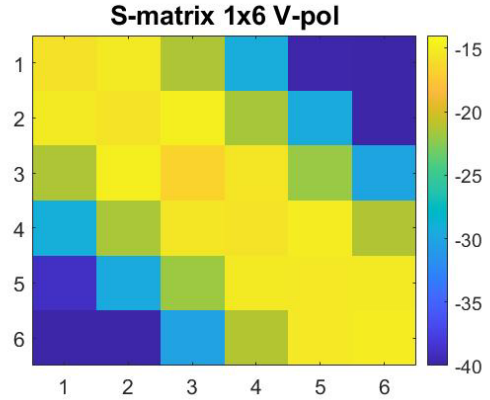
Figure 7. Measured S-matrix for ULA with vertical polarization. Element numbers displayed in horizontal and vertical axes. Colorbar units in dB.
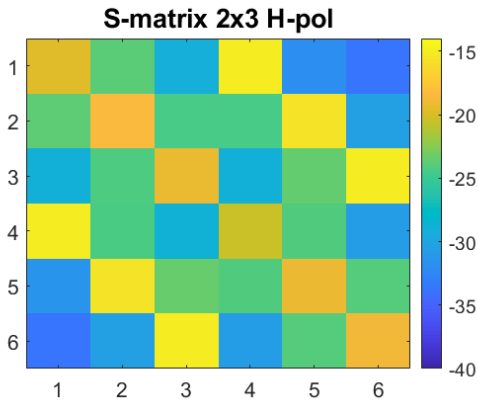
Figure 8. Measured S-matrix for UPA with horizontal polarization. Element numbers displayed in horizontal and vertical axes. Colorbar units in dB.

Figure 9. Measured S-matrix for UPA with vertical polarization. Element numbers displayed in horizontal and vertical axes. Colorbar units in dB.

between radiators 1 and 4 (top and bottom left elements as seen in Fig. 5), 2 and 5 (top and bottom centered elements shown in Fig. 5), and 3 and 6 (top and bottom right elements from Fig. 5). For the vertical polarization, as seen in Fig. 9, the maximum coupling values are observed between elements 1–3 and 4–6, as seen in Fig. 5.

The ARC is estimated from (1), for a specific geometric configuration and a selected polarization, with known excitations and the use of previously measured S-parameters (for the corresponding case). Also, a direct calculation methodology of the ARC for element n is obtained using the measured reverse (b_n) and forward (a_n) waves with the DDCs as described in Section 2 and (1).

The formulation for the estimated total transmitted fields of a MIMO emission in the far-field is obtained from (2) [32]

$$E(u, v) \approx f^i(u, v) \sum_n (1 - \Gamma_n^a) a_n e^{jk(x_n u + y_n v)} \tag{2}$$

where $e^{jk(x_n u + y_n v)}$ accounts for element positions, geometrical configuration, and inter-element spacing between elements, with the coordinates of each element on the xy-plane represented by (x_n, y_n), $u = \sin\theta\cos\phi$ and $v = \sin\theta\sin\phi$, the complex amplitude excitations given by a_n, Γ_n^a represents the estimated ARC at element n, and $f^i(u, v)$ is the isolated element pattern. For this analysis $f^i(u, v)$ is predicted for both polarizations from [40] using SENTRi, a full wave CEM tool [41].

The following section introduces the waveforms used in this work and assesses the performance impact of the total radiated fields for different cases. In addition will provide a validation of the analytical methodology by comparing with real data.

4. TRANSMITTING WAVEFORMS AND ANALYSIS

A radar waveform can be classified into a continuous wave (CW) or a pulsed wave. Out of these two waveform types, we only consider pulsed waves [19]. Specifically, in this work, we use the representation known as a complex baseband signal as transmit waveform

$$s(t) = a(t) e^{j\theta(t)} \tag{3}$$

where $a(t)$ is the amplitude modulation, and $\theta(t)$ models any phase or frequency modulation [42].

In the following sub-sections, we will examine different transmitting waveforms to study their impact in the total radiated MIMO radar fields. The analysis begins with LFM and finalizes with DDMA.

4.1. Linear Frequency Modulation

To set the stage for the study, we first analyze the LFM pulse also known as a chirp using $a(t) = 1$ and $\theta(t) = \pi B t^2 / \tau$ in (3), where an LFM can be represented as

$$s_{\text{LFM}}(t) = e^{j\pi B t^2 / \tau} \quad \text{for} \quad 0 \le t \le \tau \tag{4}$$

where bandwidth $B = 40\,\text{kHz}$ and τ represents the duration of the chirp.

We begin our analysis assessing the impact of the LFM waveforms on the ARC. As stated before, for a fixed geometric configuration and polarization, the estimated ARC at element n was calculated using (1), with the measured S-matrix and the complex amplitudes a_n and a_m from the LFM waveforms. In addition, the measured ARC was directly calculated from the recorded forward and reverse waves collected through the DDCs and BEEMER. Tables 2 and 3 present ARC estimates vs. measurements when ULA and UPA geometric configurations for horizontal and vertical polarizations are considered. It is apparent from both tables that the estimated ARC values are a good approximation of the measurements. It is also seen that the values of the ARC varies with the geometric configuration of the array and the polarization.

We continue with the analysis on the total radiated fields. The concept of pattern multiplication can be approximated from (2) with $f^i(u, v) = 1$ (isotropic pattern), $\Gamma_n^a = 0$ (ignoring mutual coupling),

Table 2. Estimated and measured ARC for LFM transmissions on a 1×6 ULA with horizontal and vertical polarizations [dB].

Channel	Estimated ARC H-pol	Measured ARC H-pol	Estimated ARC V-pol	Measured ARC V-pol
1	-16.4	-16.3	-11.9	-13.1
2	-13.1	-13.1	-6.4	-7.9
3	-13.3	-16.2	-9.9	-12.9
4	-13.6	-15.2	-7.3	-8.1
5	-12.1	-13.7	-8.2	-10.1
6	-16.4	-18.9	-10.7	-12.1

Table 3. Estimated and measured ARC for LFM transmissions on a 2×3 UPA with horizontal and vertical polarizations [dB].

Channel	Estimated ARC H-pol	Measured ARC H-pol	Estimated ARC V-pol	Measured ARC V-pol
1	-10.5	-11.9	-11.8	-12.9
2	-8.8	-9.5	-6.1	-7.9
3	-10.7	-13.6	-12.1	-15.2
4	-9.6	-11.3	-11.4	-13.3
5	-10.7	-12.6	-6.1	-8.3
6	-8.8	-10.7	-10.9	-13.0

and $a_n = 1 \, \forall n$ (uniform excitations), as shown through the normalized fields in Fig. 10. It was verified that (2) converges to the array factor (AF) obtained from [43]

$$\text{AF} = \sum_{n=1}^{N} e^{j(n-1)\psi} \tag{5}$$

with $\psi = kd\cos(\gamma + \beta)$, and he wave number $k = 2\pi/\lambda$, N is the number of elements in the array, d the spacing between elements (0.5λ), γ the angle between the array (x-axis) and a radial vector from the origin to the observation point ($\cos^{-1}(\sin\theta\cos\phi)$), and β the progressive phase between elements (chosen to be equal to zero).

Figure 11 is obtained with (2) for a ULA with unitary excitations ($a_n = 1 \, \forall n$). But this time using the V-pol estimated ARC Γ_n^a, at each element from Table 2 and the isolated element pattern $f^i(u, v)$, modeled with SENTRi as described in Section 3. The differences between Fig. 10 and Fig. 11 reveal that the total radiated fields are affected when the coupling between elements and the antenna element type are considered. It appears that the null locations were not changed ($u = \pm 0.4$, $u = \pm 0.6$), but the energy on the main lobe of Fig. 11 is more centered in $u = 0$, and the first sidelobe level decreases by -12 dB.

Figure 12 and Figure 13 present normalized power measured vs. predicted data for azimuth cuts. The measured data, depicted with dotted lines, was collected with BEEMER when the system transmitted copies of an LFM waveform from each element n. This is equivalent to a uniformly excited array in time. Then the predicted data (represented with solid lines) was obtained using (2) transmitting the same LFM waveform using (4) for modeling the excitation a_n from each element n, the estimated ARC, Γ_n^a, from Tables 2 (for Fig. 12) and 3 (for Fig. 13), and the isolated element pattern, $f^i(u, v)$, modeled with SENTRi. Blue lines depict horizontal polarization whereas black lines show vertical polarization. The solid red line seen in Fig. 12 depicts the predicted baseline obtained from (5). This
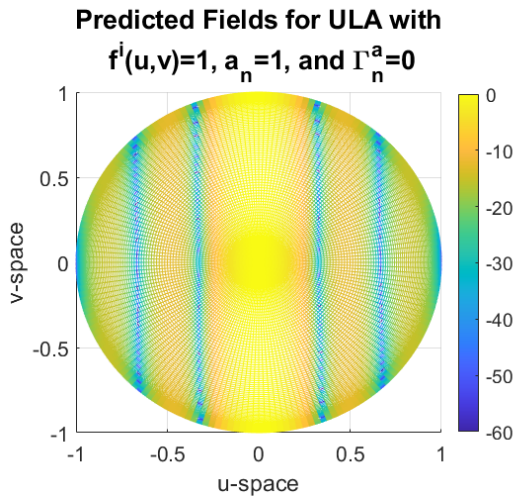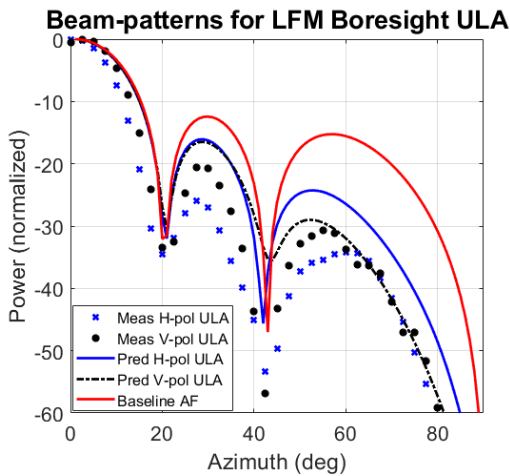
Figure 10. Normalized predicted fields for an ULA of 6 isotropic pattern, uniform excitations, and neglecting mutual coupling. Colorbar units in dB.
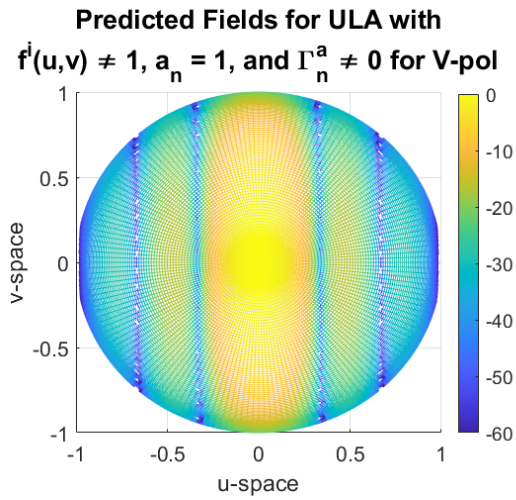

Figure 11. Approximated normalized radiated fields of a MIMO radar considering mutual coupling, the isolated radiation pattern for vertical polarization, applying uniform excitations, (2). Colorbar units in dB.

normalized baseline curve follows the theory in [44] with a -12 dB difference between the main lobe and the first sidelobe. Since we are plotting normalized power plots the predicted lines are very close within the main lobe region and the effects of the ARC and the isolated element pattern are observed through a decrease on the sidelobe levels. For both Figs. 12 and 13 the difference between the curves grow as the azimuth angle approaches towards endfire, revealing the impact of mutual coupling and polarization. We expected the measured lines to be close to the predicted curves, but not exact. This difference is, in part, due to unaccounted edge effects in the modeling of the isolated element pattern, but captured on the measured data [45]. The effects that the geometric configuration has on the normalized power curves can be seen when comparing Fig. 12 with Fig. 13.

Figure 12. Normalized measured vs. predicted radiated fields for ULA, horizontal and vertical polarizations.
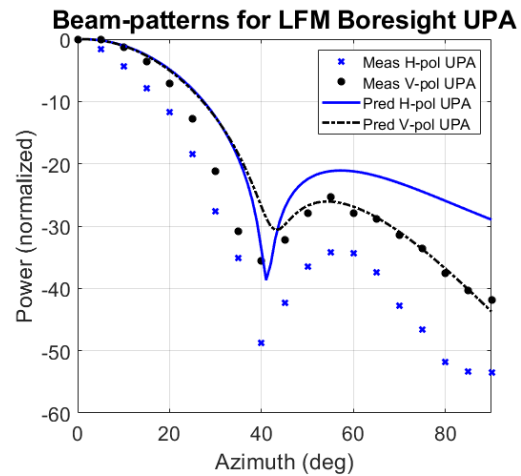
Figure 13. Normalized measured vs. predicted radiated fields for UPA, horizontal and vertical polarizations.

4.2. Doppler Division Multiple Access

The DDMA waveform for the mth element is defined as (6) [46]. DDMA is a type of frequency division multiple access modulation, where each waveform has a frequency separation much smaller than the transmission bandwidth

$$s_{\text{DDMA}}(t) = a(t)e^{j(2\pi f_m t + \psi_m)} \tag{6}$$

where ψ_m is the initial phase; f_m is the frequency separation; $a(t)$, described in (7), is a pulse train of some complex-baseband waveform $z(t)$ of duration T with T_p pulse repetition interval (PRI), where $T < T_p$. In this paper, the original waveform set has six pulses. The orthogonality of DDMA is observed in the *slow time* dimension.

$$a(t) = \sum_i z(t - iT_p) \tag{7}$$

DDMA waveforms were generated and optimized by following the methodology described by the authors in [36]. The original set of waveforms is assumed to have a coupled power greater than the desired $-10\,\text{dB}$ down from the maximum forward power on a single element, on all or some of the radiators during the emissions. With this assumption, a new set of waveforms was generated via convex optimization where the amount of coupled power was constrained while ensuring minimum changes to the original set of waveforms. The optimized set of waveforms is obtained via the minimization of a Quadratically-Constrained Quadratic Programming (QCQP) convex optimization problem formulation.

The coupled power can be expressed as a reverse wave in (8)

$$b_n = \sum_{k=0}^{M-1} S_{mn} a_n \tag{8}$$

with amplitude a_n at element n, and S-matrix S_{mn}. The coupled power can be expressed in vector form as $b_m = S_m^H a_n$. Since $|b_m|^2$ is proportional to reverse power, the desired minimum coupled energy threshold was established through (9)

$$|b_m|^2 = |S_m^H a_n|^2. \tag{9}$$

The coupled power is calculated from the recorded reverse waves. The calculated coupled power obtained from the original (Fig. 14) and optimized (Fig. 15) waveform sets for the UPA configuration with horizontal polarization are presented for the six elements and for the six pulses. For each pulse generated with the original waveform set at least one element showed a coupled power larger than $-10\,\text{dB}$, as shown in Fig. 14.
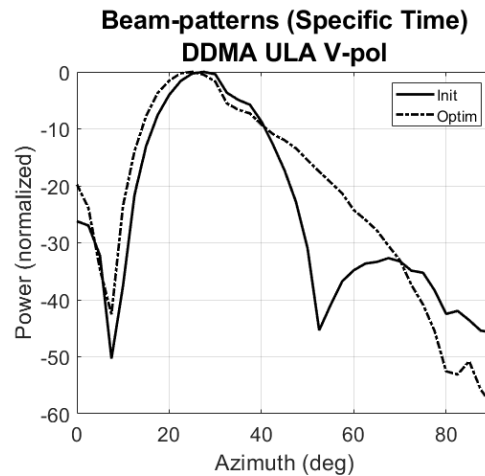
However, after optimizing the waveform set, the coupled power calculated using the optimized waveform set drops to values below $-10\,\text{dB}$, as seen in Fig. 15. The optimization method applied in
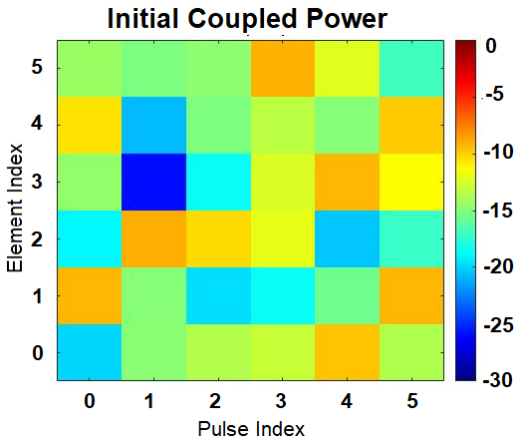
Figure 14. DDMA UPA horizontal polarization, initial coupled power.
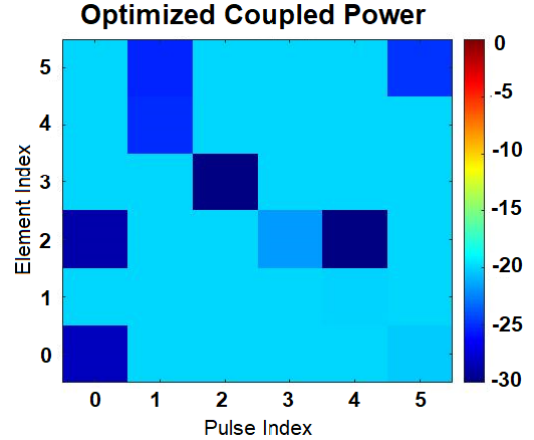
Figure 15. DDMA UPA horizontal polarization, optimized coupled power.

Figure 16. DDMA ULA V-pol, initial vs. optimized beampatterns.

this work constrained the coupled power to prevent large power reflections protecting the back end. However, after the optimization process the radiated field loses resolution as shown in Fig. 16. The solid black trace displays the radiated fields generated with the initial DDMA waveforms while the dotted black trace shows the radiated fields generated with the optimized DDMA waveform. It can be seen that after the optimization of the waveform set, the main-lobe broadens and a null around 8° is seen on both traces. However, the null around 52° is no longer seen.

5. CONCLUSIONS

In this paper, we have presented a methodology to predict the total transmitted fields of a co-located MIMO radar for different cases of arbitrary waveforms and geometrical configuration. Then, we expanded on a methodology to obtain a more direct ARC estimate through simultaneous recordings of forward and reverse waves from a co-located MIMO radar. Next, we analyzed the performance impact from the total radiated fields for different cases and the ARC for the LFM case. Lastly, we upgraded the AFRL MIMO radar testbed to obtain real data of the total radiated fields and ARC while validating the methodology discussed. As is evident from the results, we have demonstrated that the coupled power and the selected excitations play an important role in the performance of the total radiated fields and directivity of the co-located MIMO radar system. The safety of the system can be maintained if we understand reverse waves and prevent large power reflections which could damage to the back-end of the system.

REFERENCES

1. LaManna, M., "Scalable low cost approach for future multifunction antennas," *IEEE Africon'11*, 2011.
2. Frazer, G. J., Y. I. Abramovich, and B. A. Johnson, "Spatially waveform diverse radar: Perspectives for high frequency OTHR," *2007 IEEE Radar Conference*, 2007.
3. Sahin, C., P. McCormick, J. Metcalf, and S. Blunt, "Power efficient multi-beam phase-attached radar and communications," *2019 IEEE Radar Conference (RadarConf)*, 2019.

4. Ravenscroft, B., P. M. McCormick, S. D. Blunt, J. Jakabosky, and J. G. Metcalf, "Tandem-hopped OFDM communications in spectral gaps of FM noise radar," *2017 IEEE Radar Conference (RadarConf)*, 2017.

5. Ravenscroft, B., P. M. McCormick, S. D. Blunt, E. Perrins, and J. G. Metcalf, "Power efficient formulation of tandem hopped radar communications," *2018 IEEE Radar Conference (RadarConf18)*, 2018.

6. McCormick, P. M., S. D. Blunt, and J. G. Metcalf, "Simultaneous radar and communications emissions from a common aperture, Part I: Theory," *2017 IEEE Radar Conference (RadarConf)*, 2017.

7. McCormick, P. M., B. Ravenscroft, S. D. Blunt, A. J. Duly, and J. G. Metcalf, "Simultaneous radar and communications emissions from a common aperture, Part II: Experimentation," *2017 IEEE Radar Conference (RadarConf)*, 2017.

8. McCormick, P. M., C. Sahin, S. D. Blunt, and J. G. Metcalf, "Physical waveform optimization for multiple-beam multifunction digital arrays," *2018 52nd Asilomar Conference on Signals, Systems, and Computers*, 2018.

9. Chiriyath, A. R., S. Ragi, H. D. Mittelmann, and D. W. Bliss, "Novel radar waveform optimization for a cooperative radar-communications system," *IEEE Transactions on Aerospace and Electronic Systems*, 2019.

10. Herschfelt, A. and D. W. Bliss, "Joint radar-communications waveform multiple access and synthetic aperture radar receiver," *2017 51st Asilomar Conference on Signals, Systems, and Computers*, 2017.

11. Gutierrez, R. M., A. Herschfelt, H. Yu, H. Lee, and D. W. Bliss, "Joint radar-communications system implementation using software defined radios: Feasibility and results," *2017 51st Asilomar Conference on Signals, Systems, and Computers*, 2017.

12. Paul, B. and D. W. Bliss, "Constant information radar for dynamic shared spectrum access," *2015 49th Asilomar Conference on Signals, Systems and Computers*, 2015.

13. Chiriyath, A. R., B. Paul, G. M. Jacyna, and D. W. Bliss, "Inner bounds on performance of radar and communications co-existence," *IEEE Transactions on Signal Processing*, Vol. 64, No. 2, 464–474, 2016.

14. Chiriyath, A. R., B. Paul, and D. W. Bliss, "Radar-communications convergence: Coexistence, cooperation, and co-design," *IEEE Transactions on Cognitive Communications and Networking*, Vol. 3, No. 1, 1–12, 2017.

15. Chiriyath, A. R., B. Paul, and D. W. Bliss, "Simultaneous radar detection and communications performance with clutter mitigation," *2017 IEEE Radar Conference (RadarConf)*, 2017.

16. Paul, B., A. R. Chiriyath, and D. W. Bliss, "Joint communications and radar performance bounds under continuous waveform optimization: The waveform awakens," *2016 IEEE Radar Conference (RadarConf)*, 2016.

17. Rong, Y., A. R. Chiriyath, and D. W. Bliss, "MIMO radar and communications spectrum sharing: A multiple-access perspective," *2018 IEEE 10th Sensor Array and Multichannel Signal Processing Workshop (SAM)*, 2018.

18. Jakabosky, J., P. Mccormick, and S. D. Blunt, "Implementation and design of physical radar waveform diversity," *IEEE Aerospace and Electronic Systems Magazine*, Vol. 31, No. 12, 26–33, 2016.

19. Blunt, S. D. and E. L. Mokole, "Overview of radar waveform diversity," *IEEE Aerospace and Electronic Systems Magazine*, Vol. 31, No. 11, 2–42, 2016.

20. Paul, B., A. R. Chiriyath, and D. W. Bliss, "Survey of rf communications and sensing convergence research," *IEEE Access*, Vol. 5, 252–270, 2017.

21. Gupta, I. and A. Ksienski, "Dependence of adaptive array performance on conventional array design," *IEEE Transactions on Antennas and Propagation*, Vol. 30, No. 4, 549–553, 1982.

22. Gupta, I. J. and A. A. Ksienski, "Prediction of adaptive array performance," *IEEE Transactions on Aerospace and Electronic Systems*, Vol. 19, No. 3, 380–388, 1983.

23. Gupta, I. and A. Ksienski, "Effect of mutual coupling on the performance of adaptive arrays," *IEEE Transactions on Antennas and Propagation*, Vol. 31, No. 5, 785–791, 1983.

24. Yeh, C., M. Leou, and D. R. Ucci, "Bearing estimations with mutual coupling present," *IEEE Transactions on Antennas and Propagation*, Vol. 37, No. 10, 1332–1335, 1989.

25. Hui, H. T., "Improved compensation for the mutual coupling effect in a dipole array for direction finding," *IEEE Transactions on Antennas and Propagation*, Vol. 51, No. 9, 2498–2503, 2003.

26. Pasala, K. M. and E. M. Friel, "Mutual coupling effects and their reduction in wideband direction of arrival estimation," *IEEE Transactions on Aerospace and Electronic Systems*, Vol. 30, No. 4, 1116–1122, 1994.

27. Pozar, D. M., "The active element pattern," *IEEE Transactions on Antennas and Propagation*, Vol. 42, No. 8, 1176–1178, 1994.

28. Abbasi Arand, B., A. Bazrkar, and A. Zahedi, "Design of a phased array in triangular grid with an efficient matching network and reduced mutual coupling for wide-angle scanning," *IEEE Transactions on Antennas and Propagation*, Vol. 65, No. 6, 2983–2991, 2017.

29. Babur, G., P. J. Aubry, and F. Le-Chevalier, "Antenna coupling effects for space-time radar waveforms: Analysis and calibration," *IEEE Transactions on Antennas and Propagation*, Vol. 62, No. 5, 2572–2586, 2014.

30. Arnold, B. T. and M. A. Jensen, "The effect of antenna mutual coupling on mimo radar system performance," *IEEE Transactions on Antennas and Propagation*, Vol. 67, No. 3, 1410–1416, 2019.

31. Schmid, C. M., C. Pfeffer, R. Feger, and A. Stelzer, "An FMCW MIMO radar calibration and mutual coupling compensation approach," *2013 European Radar Conference*, 2013.

32. Savy, L. and M. Lesturgie, "Coupling effects in MIMO phased array," *2016 IEEE Radar Conference (RadarConf)*, 2016.

33. Colon-Diaz, N., J. G. Metcalf, D. Janning, and B. Himed, "Mutual coupling analysis for colocated MIMO radar applications using CEM modeling," *2017 IEEE Radar Conference (RadarConf)*, 2017.

34. Colon-Diaz, N., D. Janning, T. Corigliano, L. Wang, and J. Aberle, "Measurement of active reflection coefficient for co-located MIMO radar using dual directional couplers," *2018 AMTA Proceedings*, 2018.

35. Zhang, C., Q. Lai, and C. Gao, "Measurement of active S-parameters on array antenna using directional couplers," *2017 Asia Pacific Microwave Conference*, 2017.

36. Colon-Diaz, N., P. McCormick, D. Janning, and D. Bliss, "Compensation of mutual coupling effects for co-located MIMO radar applications via waveform design," *International Radar Conference*, 2019.

37. Mealey, T. C. and A. J. Duly, "Beemer: A firmware-tuned, software-defined MIMO radar testbed," *IEEE International Symposium on Phased Array Systems Technology*, Waltham, MA, USA, 2017.

38. *S-parameter Measurements*, 2019. [Online]. Available: www.keysight.com.

39. Pozar, D. M., *Microwave Engineering*, 4th Editon, Wiley, Hoboken, 2011.

40. Baumen, B., A. Christianson, A. Wegener, and W. Chappell, "Dynamic visualization of antenna patterns and phased-array beamsteering," *IEEE Antennas and Propagation Magazine*, Vol. 54, No. 3, 184–198, 2012.

41. Jin, J. and D. J. Riley, *Finite Element Analysis of Antennas and Arrays*, Wiley, New York, NY, 2009.

42. Richards, M. A., *Fundamentals of Radar Signal Processing*, 2nd Editon, McGraw-Hill Education, 2014.

43. Balanis, C., *Antenna Theory Analysis and Design*, 4th Editon, John Wiley and Sons, Hoboken, 2016.

44. Stutzman, W. and G. Thiele, *Antenna Theory and Design*, 2nd Editon, John Wiley and Sons, Hoboken, 1997.

45. Lee, S. and J. Lee, "Active element pattern and array pattern of patch array antenna including ground edge effect," *2017 International Symposium on Antennas and Propagation ISAP*, 2017.

46. Rabideau, D. J., "Doppler offset waveforms for MIMO radar," *IEEE Radar Conference*, 2011.